Atmos. Chem. Phys. Discuss., 14, 18421–18459, 2014
www.atmos-chem-phys-discuss.net/14/18421/2014/
doi:10.5194/acpd-14-18421-2014

Atmospheric Chemistry and Physics Discussions

Can IASI be used to simulate the total spectrum of outgoing longwave radiation?

E. C. Turner[1], H.-T. Lee[2], and S. F. B. Tett[1]

[1]School of Geosciences, University of Edinburgh, Edinburgh, UK
[2]Earth System Science Interdisciplinary Center, University of Maryland, College Park, Maryland, USA

Received: 4 June 2014 – Accepted: 21 June 2014 – Published: 11 July 2014

Correspondence to: E. C. Turner (e.c.turner-2@sms.ed.ac.uk)

Published by Copernicus Publications on behalf of the European Geosciences Union.

Abstract

A new method of deriving high-resolution top-of-atmosphere spectral radiances over the entire outgoing longwave spectrum of the Earth is presented. Correlations between selected channels of the Infrared Atmospheric Sounding Interfermeter (IASI) on the MetOp-A satellite and simulated unobserved wavelengths in the far infrared are used to estimate radiances between 25.25–644.75 cm^{-1} at 0.5 cm^{-1} intervals. The same method is used in the 2760–3000 cm^{-1} region. Total integrated all-sky radiances are validated with broadband measurements from the Clouds and the Earth's Radiant Energy System (CERES) instrument on the Terra and Aqua satellites at simultaneous nadir overpasses, revealing mean differences that are 0.3 $W m^{-2} sr^{-1}$ (0.5 % relative difference) lower for IASI relative to CERES with significantly lower biases in nighttime – only scenes. Averaged global data over a single month produces mean differences of about 1 $W m^{-2} sr^{-1}$ in both the all and the clear-sky (1.2 % relative difference). The new high – resolution spectrum is presented for global mean all and clear skies where the far infrared is shown to contribute 47 and 44 % to the total OLR respectively, which is consistent with previous estimates. In terms of spectral cloud radiative forcing, the FIR contributes 19 % and in some subtropical instances appears to be negative, results that would go un-observed with a traditional broadband analysis.

1 Introduction

By lieu of the fact that different thermal wavelengths are sensitive to different atmospheric components, remotely sensed hyperspectral and narrowband radiance measurements contain valuable information about atmospheric, surface and cloud properties, and also reveal fingerprints of long-term climate trends (Harries et al., 2001). Additionally they have a unique value in evaluating climate models (Goody et al., 1998). As such there is a need for detailed and complete satellite observations of terrestrial outgoing longwave radiation (OLR) in the 0–3000 cm^{-1} wavenumber range (3–1000 µm

ACPD
14, 18421–18459, 2014

wavelength) at the spectral level (Anderson et al., 2004). At the present time however, there is no satellite instrument in operation that isolates a substantial part of the OLR with the longest wavelengths, known as the Far Infrared (FIR).

The FIR, which we define as those wavenumbers between 0–650 cm^{-1} (15–1000 µm), is modulated by water vapour absorption in the pure rotation band and, to a lesser extent, the water vapour continuum. For the all-sky Harries et al. (2008) estimate that about 45 % of the total OLR from the Earth is from the FIR. Although individual transitions in this region are low in energy because rotational transitions are lower in characteristic frequency than vibrational transitions, the combined intensity of outgoing radiance at these wavelengths is large and absorption is so strong that over much of the FIR the troposphere is nearly opaque. For this this reason emissions occur mostly in the upper tropospheric and stratospheric regions.

A number of potential uses arise from resolving the FIR with satellite measurements (Mlynczak et al., 2004). Currently retrievals of upper tropospheric water vapour (UTWV) by space-borne instruments exclusively focuses on the vibrational-bending mode (ν_2) which is centred at 1595 cm^{-1} (6.3 µm). However, research has shown that the radiance from the rotational mode may be up to 6–7 times more sensitive to water vapour changes (Rizzi et al., 2002; Huang et al., 2007). Harries et al. (2008) estimate the accuracy of of the retrieval performance of the FIR to be comparable to, and sometimes slightly better than, an equivalent mid infrared sounder. Given the disproportionally large role that UTWV has in modulating the Earth's radiation balance relative to the fraction of total atmospheric water it makes up, improving the accuracy with which its vertical distribution is measured would have far-reaching benefits. Additionally, continuum absorption, where the absorption of radiation by water vapour varies smoothly with wavelength is an area that is still not fully understood (Shine et al., 2012), and recent case studies have identified discrepancies in the strength of FIR continuum of up to 50 % from estimates based on theory (Green et al., 2012). In a warmer world there will be an increase in water vapour due to its positive feedback (Soden and Held, 2006). Given that water vapour is the most important atmospheric gas in terms of greenhouse

ACPD
14, 18421–18459, 2014

effect (Miskolczi and Mlynczak, 2004), and given that peak greenhouse forcings occur in the far infrared which implies a strong contribution in directing future climate change (Sinha and Harries, 1995), it is vitally important that we increase our understanding of the role of the FIR with global, long-term observations. Particularly as due to its complexity it is unlikely that global climate models get the impact of feedbacks on the FIR under changing climate right (Harries et al., 2008).

Cirrus clouds have a significant effect on the OLR balance as their cold tops essentially shift radiative emission to lower frequencies, with a higher proportion of the OLR coming from the FIR. The amount of emission is strongly connected with the clouds height and temperature structure (Maestri and Rizzi, 2003) so essentially clouds can be characterised by their spectral signatures. Rizzi and Mannozzi (2000) estimate that the ratio of FIR to OLR increases by an average of around 30 % from clear to cloudy instantaneous conditions. With the recent increase of available global cloud property datasets afforded by the range of instruments on the A-Train satellite group, there is a need to gain corresponding complete descriptions of the clouds in terms of their spectrally resolved radiative properties, including over the FIR.

Current operational space borne hyperspectral sounders such as the Atmospheric Infrared Sounder (AIRS) (Chahine et al., 2006) or the Infrared Atmospheric Sounding Interfermeter (IASI) (Blumstein et al., 2004) have been designed to measure only the mid infrared part of the OLR. Photons at FIR frequencies have lower energies than typical band gap energies so suitable photodiodes are difficult to make. Mercury Cadmium Telluride (HgCdTe) detectors such as those used within the IASI instrument can be designed for lower frequencies however a 650 cm^{-1} cut off is common due to the enhanced sensitivity required to measure below this threshold. In order to maintain the high signal to noise ratio the detector needs to be cooled significantly to reduce the number of photons generated by the detector itself and achieve the precision required. Microwave satellite detectors such as the Microwave Limb Sounder (MLS) or the Advanced Microwave Sounding Unit (AMSU) sense wavelengths that fall just longer than the FIR, however they use very different radiance measurement technologies. Both of

ACPD
14, 18421–18459, 2014

these restrictions from either side of the FIR result in an unmeasured segment of electromagnetic radiation that has generally only been observed as part of the total infrared radiation by broadband devices.

Currently the only spaceborne instrument to spectrally resolve part of the FIR has been the Infrared Interferometer Spectrometer (IRIS) which flew onboard the Nimbus 3 and Nimbus 4 satellites in 1969 and 1970, respectively (Hanel et al., 1972). It had a minimum wavenumber of 400 cm^{-1} (25 µm) and a spectral resolution of 2.8 cm^{-1}. Since then, a limited number of instruments have been developed to measure part of, or all of, the FIR. Some have been part of balloon-borne and ground-based campaigns, such as the Atmospheric Emitted Radiance Interferometer (AERI) (Turner et al., 2004), and the Radiation Explorer in the Far InfraRed (REFIR-BB/PAD) (Esposito et al., 2007), whose measurements have been used to test the representation of the FIR by line-by-line radiative transfer models (Bianchini et al., 2008). Aircraft campaigns using instruments such as the Tropospheric Airborne Fourier Transform Spectrometer (TAFTS) (Green et al., 2012), REFIR-PAD (Palchetti et al., 2008), and the Interferometer for Basic Observation of Emitted Spectral Radiance of the Troposphere (I-BEST) Masiello et al. (2012), have been used to gain insights into the FIR continuum. Though these airborne experiments do prove useful for testing parametrisations in radiative transfer models, only spaceborne instruments can give the full Earth coverage of sufficient temporal length needed for climate studies.

Recently, much work has been put into developing and testing a detector proposed for a spaceborne mission with a response in the 50–2000 cm^{-1} range at high spectral resolution (approximately 0.643 cm^{-1}). The Far-Infrared Spectroscopy of the Troposphere (FIRST) instrument (Mlynczak et al., 2004) has detectors that are cooled to 4.2 K with liquid helium to achieve the necessary sensitivity (for comparison the optical core of IASI is 91.3 K). Initial comparisons of FIRST measurements taken on balloon flights against theoretical calculations and spectral overlaps with coincident satellite instruments show excellent fidelity (Mlynczak et al., 2006), however, despite high priority recommendations (see National Research Council, 2007) there is currently no sched-

ACPD
14, 18421–18459, 2014

uled launch date for its deployment, even though it is often noted that the FIR has been measured extensively and directly on every planet in the solar system except Earth and Pluto (Hanel et al., 2003).

Historically, when part of the infrared spectrum has not been measured from space the remaining bands are often estimated through alternate means. Previous studies have sought to reproduce total OLR from narrowband and hyperspectral sounders with the combined motivations of validating current operational broadband sounders, mitigating them against potential failure and gaining wider diurnal coverage. The absence of an instrument that measured total outgoing LW flux in the late 1970's led to its estimation using a single waveband in the 800–950 cm^{-1} window region (10.5–12.5 µm) from the two-channel scanning radiometer onboard NOAA-1–NOAA-5 via a non-linear regression model derived from radiative transfer calculations applied to 99 different atmospheric profiles (Gruber, 1977; Gruber and Winston, 1978). As the reference broadband results are obtained from a radiative transfer code this method is termed "theoretical". Alternatively, Ohring et al. (1984) used the Earth Radiation Budget (ERB) broadband OLR measurements on the Nimbus 7 satellite as a reference to obtain regression coefficients between these and window band observations from the Temperature Humidity Infrared Radiometer (THIR) instrument on the same satellite at collocated footprints. This method is termed "empirical", because measured data is used as a reference.

Clearly, there are uncertainties in using only one spectral region to estimate the entire OLR. Accordingly, an outgoing LW flux product from the High Resolution Infrared Sounder (HIRS) instruments was developed in the 1980's by Ellingson et al. (1989) using multi-spectral regression between OLR and HIRS radiances simulated from a theoretical radiation model, which explained more than 99 % of the significance. This product is useful for its longevity and recent incarnations show extremely high correlations with CERES broadband data, with global mean differences less than 2 $W\,m^{-2}$ (Lee et al., 2007). Recently, Sun et al. (2010) have used the empirical approach to derive broadband data from AIRS using the CERES outgoing LW flux to generate re-

ACPD
14, 18421–18459, 2014

gression coefficients from principal component scores of AIRS radiances. The AIRS OLR therefore is based empirically on OLR estimates from CERES, and as such mean biases between the two products are low (0.26 $W m^{-2}$).

As regards spectrally resolved measurements in the FIR, Huang et al. (2006) used clear-sky radiances from the IRIS instrument to predict fluxes in its uncovered spectral regions below 400 cm^{-1} and above 1400 cm^{-1} by assuming a linear relationship between those regions and fluxes in the H_2O ν_2 band and a narrow window region. Regression coefficients between measured and unmeasured wavebands were obtained from calculated radiances using the MODTRAN radiative transfer model applied to simulated profiles from the GFDL AM2 global climate model. These coefficients were then applied to IRIS to simulate the whole OLR. The authors found mean differences of 0.72 $W m^{-2}$ between IRIS OLR and fluxes produced from ECMWF ERA-40 reanalysis data for the tropical oceans, but noted that when the analysis is broken down by wavelength biases are larger but of opposite signs so compensate overall. Huang et al. (2008) adapted this theoretical method for the hyperspectral Atmospheric Infrared Sounder (AIRS) to derive spectral fluxes in its uncovered wavebands using principle component analysis. A complete set of clear-sky fluxes from 10 to 2000 cm^{-1} were calculated at 10 cm^{-1} intervals, and validated with broadband observations using collocated CERES data. Annual mean differences of 0.67 $W m^{-2}$ were found over the tropical oceans for 2004. A corresponding analysis for cloudy pixels yielded equivalent differences of 2.15 $W m^{-2}$ (Huang et al., 2010) and similar analyses revealed differences of up to 1.73 and 3 $W m^{-2}$ for the clear and all-sky respectively, depending on the year examined (Huang et al., 2013). Chen et al. (2013) extended this work to include land and extra-tropical ocean pixels and found global mean differences of 0.96 $W m^{-2}$ for the daytime, and 0.86 $W m^{-2}$ for nighttime using clear-sky data only. In lieu of the lack of complete FIR observations we follow the approach taken by previous studies and develop an algorithm to "fill in the gaps" of the available data. The high-resolution IASI instrument is used, which was originally designed to fulfil both the meteorology requirements of high spatial coverage, and the atmospheric chemistry needs of accu-

ACPD
14, 18421–18459, 2014

racy and detailed vertical resolution (Clerbaux et al., 2009). IASI has 4 times as many channels as the AIRS instrument for the same range of thermal infrared wavelengths, and is free from gaps over the whole spectral range. It is part of the payload of the MetOp-A satellite, which provides a differently timed polar orbit and hence a different sampling of the diurnal cycle to existing satellites that carry broadband instruments.

We use a theoretical based regression technique similar to the one used to derive OLR from the HIRS instrument based on physical atmospheric profiles which is described in Sect. 2.2. In order to verify the calculated IASI OLR product we perform an independent comparison with broadband instruments on other satellites, which avoids the introduction of compounded errors from radiative transfer model evaluations. Section 2.4 explains how times and locations are identified where the path of MetOp-A crosses those of the Aqua and Terra satellites, both of which carry CERES instruments. By restricting this set further to nadir-like views the instruments will sense the same scene at the same time, providing the opportunity for indirect validation of the new IASI OLR product. Results of this, and a global composite comparison, are presented in Sects. 3.1 and 3.2 respectively. Finally the complete constructed OLR spectrum is presented in the remaining Sects. 4.1, 4.2 and 4.3. In this study no attempt has been made to translate unfiltered IASI radiances to fluxes avoiding the need to involve angular distribution models (ADMs) at this stage. ADMs are empirical relationships between radiances measured at a single angle to irradiance estimated over all angles (Loeb et al., 2003), and as such introduce a further level of uncertainty into the validation, which can be up to 2.3 % (Instantaneous LW TOA flux: see the CERES Terra Edition3A SSF Data Quality Summary). This also allows for a cleaner comparison with climate model simulated satellite products in the future. Therefore, the abbreviation OLR refers to the total LW radiance product herein.

ACPD
14, 18421–18459, 2014

2 Data and methodology

2.1 IASI level 1c and combined sounding products data set

The IASI Flight Model 2 (FM2) instrument is onboard the MetOp-A satellite launched by EUMETSAT in October 2006 and operates in a sun-synchronous orbit. It is a 8461 channel passive sounder that measures in the mid infrared spectral region between 645–2760 cm^{-1} (3.62–15.5 µm) at a 0.25 cm^{-1} sampling interval with no gaps. The apodised level 1c radiances have a 0.5 cm^{-1} resolution. The effective field of view (EFOV) is a 2×2 matrix of 4 circular instantaneous fields of view (IFOV) that each have an approximate footprint diameter of 12 km at nadir. There are 30 EFOV per scan line which takes 8 s to complete and had a maximum scan angle of 48.3° in the across track direction. In its nominal mode IASI uses a view of an internal blackbody and deep space once every scanline to calibrate on-board, as described by Simeoni et al. (2004). It is thought to have an average absolute radiometric accuracy of 0.5 K, measured in brightness temperature (personal communication with EUMETSAT).

We restrict the data to the IFOVs with the smallest satellite zenith angles in order to retain only nadir looking pixels. There are 4 IFOVs with angles less than 1.5° which are indices 57, 58, 63 and 64 in the across track direction have viewing angles of approximately 1.34°, 1.37°, 1.41°, and 1.39° respectively. Alongside the level 1c radiances clear-sky flags are obtained from the level 2 combined sounding products to construct an equivalent clear-sky product. Cloud detection in IASI pixels is performed from a choice of 5 separate tests, involving window channels, AMSU-A, AVHRR and CO_2 slicing, depending on the quality of the input data.

2.2 Method for estimating OLR from IASI

Strong correlations can be found between frequencies in the LW spectra with similar spectroscopic properties. Unmeasured radiances with FIR wavenumbers between 25 and 650 cm^{-1} and those between 2760 and 3000 cm^{-1} (which we will term near in-

ACPD
14, 18421–18459, 2014

frared (NIR) radiances) can be estimated from IASI observations. For example, FIR wavenumbers in the strong H_2O rotational band such as 25.25 cm^{-1} can have strong correlations with those in the centre of the 667 cm^{-1} CO_2 and 1533 cm^{-1} H_2O ν_2 bands by virtue of their similar sensitivity to high altitude temperatures (Fig. 1). However the 1533 cm^{-1} band is physically more similar to frequencies in the FIR and therefore has comparably larger correlations.

Adapting the simulation methodology of Ellingson et al. (1989), the Line-By-Line Radiative Transfer Model (LBLRTM) (Clough et al., 1992, 2005) available publicly at http://rtweb.aer.com, is used to simulate LW spectra over the spectral range 25–3000 cm^{-1} at a 0.5 cm^{-1} sampling interval with radiosonde data from 1600 soundings (Phillips et al., 1988). A second set of cloudy simulations is obtained by inserting a cloud at a particular level (randomly distributed). Several regression model formulations were investigated for the purpose of NIR/FIR radiance prediction. A log–log transformation was found to provide the optimal performance in minimization of estimation errors and regression residual distributions. This empirical behaviour can also be explained physically, as transmittances will be approximately linear. Figure 2 shows an example of the log–log relationship between radiances at 33.75 cm^{-1} and the channel that has a maximum correlation with it (2091.25 cm^{-1}). Root mean square errors are about 0.4 % for all angles.

The best predictor channels are selected as those with maximum correlation coefficients between the log-radiances (Fig. 3) and then the corresponding regression coefficients are found (Fig. 4). For this application the local zenith angle is restricted to the nadir cases. The prediction equation to estimate the radiance $I_{\nu_{\mathrm{FIR/NIR}}}$ in either the FIR or NIR regions at wavenumber ν can be written as,

$$\ln(I_{\nu_{\mathrm{FIR/NIR}}}) = a_0 + a_1 \ln(I_{\nu_{\mathrm{predictor}}}) \quad (1)$$

where $I_{\nu_{\mathrm{predictor}}}$ is the radiance observed by IASI at the predictor wavenumber (W m^{-2} sr^{-1} $(cm^{-1})^{-1}$) and a_0 and a_1 are the calculated regression coefficients.

ACPD
14, 18421–18459, 2014

2.3 CERES Single Scanner Footprint (SSF) Ed3A

The broadband OLR product constructed from the extended IASI radiances is compared with existing CERES products. CERES SSF Edition 3A dataset is obtained from the Atmospheric Science Data Center at the NASA Langley Research Center for both the Terra and Aqua polar orbiting satellites (Wielicki et al., 1996). In the cross-track scanning mode there are 90 FOVs in a single scanline that each consist of a circular pixel measuring 20 km diameter at nadir. The swath takes 6.6 s to complete and has a maximum scan angle of 65.8°. For the present study only pixels with the minimum satellite zenith angles, which are less than 1° (FOV 45 and 46) are selected to retain only nadir-looking views. Cloud properties for CERES instruments are inferred from the Moderate-Resolution Imaging Spectroradiometer (MODIS) imager which flies onboard the same satellites, and are based on threshold tests with adjacent channels (Minnis et al., 2004). Each satellite carries 2 identical CERES instruments. For the data acquired, Flight Model 1 (FM1) on Terra and Flight Model 3 (FM3) on Aqua are operational in the cross-track mode.

CERES measures filtered radiances in terms of physical origin, rather than wavelength, however approximate boundaries for the 3 channels are reflected shortwave (SW) (0.3–5 µm), total (0.3–200 µm), and window (8–12 µm). LW radiation is determined from a weighted combination of measurements from the other channels and hence all emitted thermal radiances that fall within the 0.3–200 µm (50–> 3000 cm^{-1}) range are included.

Relative errors due to the process of unfiltering radiances are found to be generally less than 0.2 % in the LW (Loeb et al., 2001). The uncertainty in net TOA flux due to absolute calibration uncertainty is 2 % in the SW channel and 1 % in the total channel at the 95 % confidence level (Priestley et al., 2002). Since nighttime LW radiation is based only on the total channel the uncertainties are essentially the same at 1 %. For the daytime combining the uncertainties of the SW channel yields an estimate of around 2.1 %, which produces an average daily LW uncertainty of 1.5 % (see Appendix

ACPD
14, 18421–18459, 2014

of Loeb et al., 2009, for the derivation). The same percentage value holds for both flux and radiance because they are in a proportional relationship by definition.

Determining absolute radiometric calibration uncertainty once in-orbit is dependent on a reference instrument and it remains a challenge to achieve a reference traceable to international standards. This is a problem of such critical importance that it led to the formation of an international effort called the Global Space-based Intercalibration System (GSICS) (Goldberg et al., 2011). The current CERES Edition-3 product established FM1 as the reference to place all the CERES instruments of the same radiometric scale, and as such will contain fewer correction uncertainties. All flight models were corrected for spectral darkening at shorter wavelengths (< 1 µm) due to UV exposure which caused degradation in both the SW channel and the shorter wavelength region of the total sensors. Studies that use an edition of CERES prior to Edition 3 will be subject to this error, which overestimates flux by as much as a 0.8 % (CERES LW flux daytime for FM1 and FM3: see the CERES Terra and Aqua Edition3A SSF Data Quality Summary). Further refinements for the spectral correction have been proposed for the CERES Edition 4 production (Thomas and Priestley, 2014). This revision is expected to improve the accuracy and stability of CERES data, particularly over the daytime land scenes. The present study uses CERES Edition 3 data and as such, it is important to be aware of the possible errors relating to this version.

Overall, each algorithm step in new editions adds its own uncertainty so the estimates quoted above are taken here as lower bounds.

2.4 Identifying simultaneous nadir overpasses

Two satellites in sun-synchronous polar orbits with different equatorial crossing times will cross at the polar regions at approximately the same north/south latitude each time. When radiometers from both satellites view the same nadir scene at the same time this is called a simultaneous nadir overpass (SNO). Using SNOs are preferable to comparing composite measurements over the same time period because individual scene differences between cloud and surface properties are avoided. This study

ACPD
14, 18421–18459, 2014

uses the database of predicted SNOs provided by the National Calibration Center of NOAA; available at http://ncc.nesdis.noaa.gov/SNO/SNOs//NCC_SNOs_prediction_service.html which makes SNO predictions based on the SGP4 orbital perturbation model (Cao et al., 2004).

Aqua has local equatorial crossing times (LECTs) of 13:30 (ascending) and 01:30 (descending), and Terra has LECTs of 22.30 (ascending) and 10:30 (descending). MetOp-A has an ascending node of 21:30 and a descending node LECT of 09:30. SNOs 2012 between MetOp-A and Aqua, and MetOp-A and Terra, are first filtered following the criteria set out in the methodology of Cao et al. (2005). This specifies that at the SNO: (1) the time difference between nadir pixels is less than 30 s and, (2) the distance between nadir pixels is less than the diameter of one footprint. Based on the average of the 20 km CERES pixel and the 12 km IASI pixel this threshold is set to 16 km. This yields approximately 100 SNOs for each satellite pair over the course of a year. Using these predictions the closest matches in terms of time and distance were identified in the satellite data for the most nadir-looking field of views for each instrument. The resulting locations of IASI pixels identified as SNOs are shown in Fig. 5. By virtue of their different equatorial crossing times MetOp-A and Aqua SNOs all lie around 74° N/S and MetOp-A and Terra SNOs all lie around 81° N/S. Unfortunately SNO events for polar orbiters are restricted to the polar regions whose conditions are not representative of the whole planet, however this presents an even stricter test for the algorithm as the radiosonde data from which the line-by-line radiances were calculated were only obtained from tropical and mid-latitude scenes. We estimate the biases for the rest of the globe by additionally performing a composite comparison of OLR products in Sect. 3.2.

ACPD
14, 18421–18459, 2014

3 Validation with CERES

3.1 Instantaneous OLR at SNOs

For maximum consistency with CERES, IASI OLR radiances are cut off at the 50 cm^{-1} lower wavenumber limit, and integrated over all remaining radiances up to 3000 cm^{-1}. OLR estimates from coincident IASI and CERES pixels generally lie close together, with the majority falling within 2 $W m^{-2} sr^{-1}$ of each other (Fig. 6). In general differences will be introduced by the slightly different nadir angles and footprint sizes between CERES and IASI, and the accuracy of the colocations. Absolute values range from 30 to over 80 $W m^{-2} sr^{-1}$ yet there is no identifiable relationship between scene radiance and bias indicating the IASI algorithm is robust against profile conditions at these latitudes. Nighttime radiances show a slightly higher correlation (0.99) compared with daytime scenes (0.98). Whether the lower daytime correlation originates from errors in the SW channel involved in estimating daytime CERES OLR, solar backscatter contamination of either instrument or the increased variability of daytime OLR is beyond the scope of this study.

The same results shown as absolute biases (CERES – IASI) are presented as a time series in Fig. 7, revealing no dependency of error upon season. Table 1 breaks down these biases by CERES instrument. Mean IASI OLR values are about 0.3 $W m^{-2} sr^{-1}$ lower than CERES when all local times are considered, and individual differences are generally within ± 6 $W m^{-2} sr^{-1}$. Larger biases appear to be associated with partly cloudy or overcast scenes and are likely due to horizontal cloud inhomogeneity in the region of the SNO which can have a large effect on the height, and hence temperature/radiance of emission.

When relative differences are considered this corresponds to LW radiances that are 0.5 % higher in CERES than IASI. Split into day and nightime scenes it is apparent that this bias is dominated by daytime pixels as the mean nighttime relative error is only 0.01 % whereas daytime differences are 0.95 %. This could be related to the CERES Ed4 findings about the SRF correction determination method. All relative differences

ACPD
14, 18421–18459, 2014

are well within the uncertainty range of CERES unfiltered radiance based on absolute radiometric calibration uncertainty and relative unfiltering errors as detailed in Sect. 2.3. Given that the original correlation co-efficients between radiances were calculated using only tropical and mid-latitude profiles, the fact that the algorithm performs so well in polar regions shows that it is highly robust under different scene types.

3.2 Global composite OLR

In order to obtain an estimate of the magnitude of extra-polar biases, gridded and averaged nadir data from CERES (Aqua and Terra) for the whole month of April 2012 is compared with the equivalent constructed OLR composite from IASI (Fig. 8). For a single day there are approximately 40 000 pixels collected for each instrument, binned to a $2.5^{\circ} \times 2.5^{\circ}$ grid. Global mean biases split into day and night time scenes along with the differences between Aqua and Terra are also shown in Table 2.

The IASI OLR product continues to be underestimated with respect to CERES when the whole globe is averaged together, with a bias that is about 3 times greater than the SNO mean bias for both Aqua and Terra (0.79 and 1.04 $\mathrm{W\,m^{-2}\,sr^{-1}}$, with a relative error of 0.94 and 1.26 % respectively) in the all-sky. This increase is not wholly unexpected due to the nature of the compositing process and is likely to be dominated by diurnal variations, which is evident from the general noisiness of the data in Fig. 8. More extreme differences can be seen over land and deep cloud regions where diurnal variations are greatest. Dealing with clear-sky pixels only removes the cloudy part of this diurnal variation. On a daily basis clear-sky is identified in 15 % of the data, but when gridded and averaged over the month 70 % of the globe has clear-sky data. As CERES and IASI use different methods to detect clouds it is possible that they would interpret the cloudiness of the same scene differently thus incorporating a possible systematic bias into the clear-sky comparisons, which are all observed to be higher than their all-sky equivalents.

The difference due to the 3 h local time difference between Terra and Aqua (0.26 $\mathrm{W\,m^{-2}\,sr^{-1}}$ in the all-sky) indicates time sampling issues are not relatively sig-

ACPD
14, 18421–18459, 2014

nificant, though a longer time period would undoubtedly reveal clearer patterns. Data volume issues prohibit testing this currently. As with the SNO comparison biases between OLR products are significantly larger in the daytime which falls in line with the existing correction error identified in the Ed3 CERES data mentioned in Sect. 2.3. However, with the exception of daytime clear-sky differences between Aqua CERES and IASI, relative mean biases are still within the uncertainty ranges estimated for CERES for all time periods and given the uncontrollable factors involved in the composite process this gives us confidence that the algorithm used to estimate IASI OLR is spatially robust.

4 Spectral IASI OLR

4.1 Instantaneous spectral IASI OLR

Example instantaneous IASI OLR spectra show that the FIR contributes between 43–64 % to the total OLR depending on the scene type (Fig. 9). This is within the range of previous estimates (Harries et al., 2008). We present nighttime scenes which is when the FIR is particularly dominant as temperatures fall. In the daytime, however, higher surface temperatures often allow the window region to reach higher intensities when there is little or no cloud. In non-cloudy cases temperature is the dominating factor controlling the total intensity of LW radiance received at the TOA. For example, the spectrum over the Sahara (Fig. 9c) emits about double the total radiance as that over Antarctica (Fig. 9d). However when clouds are present their height and coverage can have a highly significant influence. For example it is certain that the temperature in the tropics will be higher than that in Antarctica, and yet Fig. 9a and d have similar values of total OLR. This is because it is likely that deep convective cloud brings the height of tropical emission to the cold upper troposphere where photons have lower energies. Clouds give more weight to the FIR as part of the OLR overall, the tropics and the desert are both warm regions and yet the FIR contributes 43 % to the clear dry case

ACPD
14, 18421–18459, 2014

and 62 % to the moist cloudy case, which is almost a third greater. Lower stratiform clouds that are prevalent over midlatitude land will not have as large an effect on the whole spectrum, but emission in the window region is still reduced with respect to the FIR (Fig. 9b) with a higher percentage coming from the FIR (49 %) than in the clear-sky desert.

4.2 Mean clear and cloudy spectral IASI OLR

When split into global mean clear and cloudy scenes an average of 47 % of the total LW radiance comes from wavenumbers less than 645 cm^{-1} when clouds are always present, and 44 % when the atmospheric column is clear (Fig. 10a). The peak wavelength of emission also shifts from 558.25 to 513.25 cm^{-1} for the cloudy only case. The NIR region constructed by a similar method contributes near-negligible radiances of 0.03 $W m^{-2} sr^{-1}$ (0.04 %) in cloudy cases and 0.05 $W m^{-2} sr^{-1}$ (0.06 %) in clear cases. This is a region of partial transparency and hence like the 800–1250 cm^{-1} window dominates more in the clear-sky.

The difference between the averaged clear and all-sky is equivalent to the effect of a cloud and is often know as cloud radiative forcing (CRF) or cloud radiative effect (CRE). Figure 10b shows CRF values for the whole LW spectrum, with a total value of 8.1 $W m^{-2} sr^{-1}$ Note that our definition of CRF is in terms of radiance, not flux. In general there is more outgoing radiation at all wavenumbers in the clear-sky because liquid clouds are nearly opaque to the whole OLR spectrum and re-emit at lower temperatures/energies than the clear-sky case. Wavebands at 0–200 cm^{-1}, 650–700 cm^{-1} and around 1500 cm^{-1} are strongly sensitive to rotational water vapour transitions, CO_2 ν_2 transitions and the vibrational ν_2 water vapour transitions respectively, and as such peak emissions are in the upper troposphere/lower stratosphere where clouds are few and hence the CRF is low. Even though in the cloudy case the FIR represents a more significant proportion of the total OLR, the clear-sky still emits more over this wavelength range in terms of absolute magnitude. Although the majority of energy in cloud

ACPD
14, 18421–18459, 2014

radiative forcing is distributed over the atmospheric window spectral interval, the FIR still accounts for 19 % of the total CRF.

4.3 Maps of OLR, FIR and window wavebands

Spatially, all-sky IASI OLR averaged over the whole month of April 2012 peaks in the clear desert and extra-tropical subsidence regions around ±20°. In the latter, low maritime clouds emit radiation at high temperatures similar to those at the surface (Fig. 11a). Deep convective clouds over the intertropical convergence zone, Indo-Pacific warm pool and monsoon regions of Africa and South America reduce OLR because emission is from high, cold cirrus cloud tops. Correspondingly these regions also have the highest CRF values (Fig. 11b), because the difference between the all and the clear-sky is at a maximum. Unexpected features of this plot are occasional negative CRF values, bordering the polar continents. These values tend not to be lower than $-1\,\mathrm{W\,m^{-2}\,sr^{-1}}$. CRF is generally a positive quantity, i.e. if a cold cloud is added to any particular clear-sky scene instantaneously the radiation emitted from the top of the cloud will be reduced with respect to the clear-sky amount. However, when a lower tropospheric temperature inversion is present, clouds can be warmer than the surface. These clouds are particularly common over the Antarctic Plateau in austral winter as a result of the snow-surface emissivity being greater than the atmospheric emissivity. Additionally cloud detection algorithms often struggle in the polar regions due to lack of thermal contrast between ice covered surfaces and cloud tops. Temperature inversions are also a prominent feature of the subtropical trade wind regimes due to adiabatic compression of subsiding warm air masses which produce shallow cumulus clouds that are warmer than the surface. Examples of this behaviour are visible in the data around ±20° in Fig. 11b.

The proportion of the OLR spectrum that falls within the FIR waveband peaks in the coldest latitudes of Antarctica as most of the outgoing photons have very low energies and hence low wavenumbers (Fig. 11c). It is also higher in regions of greater cloud cover, and this can be identified in the deep convective cloud regions with respect to

ACPD
14, 18421–18459, 2014

the surrounding clearer areas, such as over the Sahara. The FIR and the window (WIN) waveband between 800 and 1250 cm^{-1} (Fig. 11e) are inverse to one another in terms zonal variability, i.e. when the FIR contribution is higher the WIN contribution is lower and vice versa. However, the FIR contributes an average of 40 % more to the OLR overall in terms of absolute magnitude. In terms of contribution to the CRF though, the WIN is 3 times greater on average than the FIR (Fig. 11d and f), but again the patterns of zonal variability are inverse to each other. Interesting, in the subtropical subsidence regions there are some negative values of CRF in the FIR, meaning the average all-sky radiation is more than the average clear-sky at these wavenumbers. As the total OLR and the WIN CRF are still positive in (most of) these locations these cannot be attributed solely to temperature inversions. It is possible to speculate about the cause of this behaviour, for example, clear skies associated with humid conditions and trade wind inversion clouds associated with dryer conditions would result in a higher emission level for the FIR. It could also be the case that the FIR is more sensitive to a false diagnosis of a cloudy sky pixel as clear than the whole OLR spectrum overall. As a result of these negative FIR CRFs, the corresponding positive WIN CRFs peak at these locations because they are now contributing more to the positive total OLR CRF. This value is still low due these 2 parts of the spectrum cancelling with one another, something that would go un-observed with a purely broadband analysis.

5 Conclusions and discussion

In this study we have shown that IASI can be used to simulate the entire range of wavenumbers (25–3000 cm^{-1}) needed to estimate the total outgoing longwave radiation at a sampling resolution of 0.5 cm^{-1} in the far infrared (< 645 cm^{-1}) and the near infrared (> 2600 cm^{-1}). The method is based on theoretical correlations between measured and un-measured parts of the spectrum, derived using simulations from the line-by-line radiative transfer code LBLRTM applied to 3200 measured atmospheric profiles, and is independently verified by broadband instruments on other satellites. Coincident

ACPD
14, 18421–18459, 2014

all-sky measurements between IASI and CERES at simultaneous nadir overpasses in polar regions show mean differences of about 0.3 $W m^{-2} sr^{-1}$ (0.5 % relative difference), and a composite comparison of all regions gives global mean differences of about 1 $W m^{-2} sr^{-1}$ (just over 1 %) over a single month for all-sky measurements. This is within the 1.5 % absolute calibration uncertainty for LW CERES radiances, which is good considering the limited time period. When estimating the difference in units of flux a simple isotropic assumption (flux = $\pi \cdot$radiance) yields biases of 0.9 and 3.1 $W m^{-2}$ for the colocated and composite analysis respectively, which are comparable in magnitude to those presented in previous studies of all-sky OLR that are constructed in a similar manner. Given that this study uses completely independent measurements from different instruments on different satellites, and approximately 50 % of the spectrum is being estimated from our method, this is a promising result.

Instantaneous examples of the simulated spectrum show the far infrared contributes between 43–64 % to the total OLR with a global weighted average of 47 % in the all-sky and 44 % in the clear-sky. The results of our comparison are consistent with previous values proposed in the literature (45 % for the all-sky) Harries et al. (2008). This study serves as a proof of concept of the usefulness of IASI for estimating the total LW radiance and the terrestrial far infrared at an unprecedented level of spectral resolution. Quantities such as CRF which are commonly studied only as a single integrated quantity across the OLR contain much more information when examined on a spectral level.

It is feasible that this product could be developed by applying empirical angular distribution models to the radiances to give flux estimates using a similar approach taken by previous studies (e.g. Huang et al., 2008), and as such IASI has the potential to be supplementary to the broadband instrument observations. Given that IASI will eventually be carried by 3 different MetOp satellites in the same local-time orbit, and IASI-New Generation proposed for the second generation of MetOp satellites will have even higher sampling resolution (0.125 cm^{-1}) (Crevoisier et al., 2013), this provides the possibility of a product with valuable length and the ability to be inter-satellite calibrated between instruments.

ACPD
14, 18421–18459, 2014

Acknowledgements. CERES and IASI data was provided by NASA and EUMETSAT. We thank N. Loeb for valuable comments. This work was funded as part of a Ph.D. scholarship by the National Environmental Research Council of the UK.

References

Anderson, J., Dykema, J., Goody, R., Hu, H., and Kirk-Davidoff, D.: Absolute, spectrally-resolved, thermal radiance: a benchmark for climate monitoring from space, J. Quant. Spectrosc. Ra., 85, 367–383, 2004. 18423

Bianchini, G., Carli, B., Cortesi, U., Del Bianco, S., Gai, M., and Palchetti, L.: Test of far-infrared atmospheric spectroscopy using wide-band balloon-borne measurements of the upwelling radiance, J. Quant. Spectrosc. Ra., 109, 1030–1042, 2008. 18425

Blumstein, D., Chalon, G., Carlier, T., Buil, C., Hebert, P., Maciaszek, T., Ponce, G., Phulpin, T., Tournier, B., Simeoni, D., Astruc, P., Clauss, A., Kayal, G., and Jegou, R.: IASI instrument: technical overview and measured performances, in: Optical Science and Technology, the SPIE 49th Annual Meeting, International Society for Optics and Photonics, Denver, CO, 2 August 2004, 196–207, 2004. 18424

Cao, C., Weinreb, M., and Xu, H.: Predicting simultaneous nadir overpasses among polar-orbiting meteorological satellites for the intersatellite calibration of radiometers, J. Atmos. Ocean. Tech., 21, 537–542, 2004. 18433

Cao, C., Ciren, P., Goldberg, M., and Weng, F.: Intersatellite calibration of HIRS from 1980 to 2003 using the simultaneous nadir overpass (SNO) method for improved consistency and quality of climate data, Int. TOVS Study Conf., Beijing, China, May 2005, 409–414, 2005. 18433

Chahine, M. T., Pagano, T. S., Aumann, H. H., Atlas, R., Barnet, C., Blaisdell, J., Chen, L., Divakarla, M., Fetzer, E. J., Goldberg, M., Gautier, C., Granger, S., Hannon, S., Irion, F. W., Kakar, R., Kalnay, E., Lambrigtsen, B. H., Lee, S.-Y., Marshall, J. L., McMillan, W. W., McMillin, L., Olsen, E. T., Revercomb, H., Rosenkranz, P., Smith, W. L., Staelin, D., Strow, L. L., Susskind, J., Tobin, D., Wolf, W., and Zhou, L.: AIRS: improving weather forecasting and providing new data on greenhouse gases, B. Am. Meteorol. Soc., 87, 911–926, 2006. 18424

ACPD
14, 18421–18459, 2014

Chen, X., Huang, X., Loeb, N. G., and Wei, H.: Comparisons of clear-sky outgoing far-IR flux infered from satellite observations and computed from the three most recent reanalysis products, J. Climate, 26, 478–494, 2013. 18427

Clerbaux, C., Boynard, A., Clarisse, L., George, M., Hadji-Lazaro, J., Herbin, H., Hurtmans, D., Pommier, M., Razavi, A., Turquety, S., Wespes, C., and Coheur, P.-F.: Monitoring of atmospheric composition using the thermal infrared IASI/MetOp sounder, Atmos. Chem. Phys., 9, 6041–6054, doi:10.5194/acp-9-6041-2009, 2009. 18428

Clough, S., Shephard, M., Mlawer, E., Delamere, J., Iacono, M., Cady-Pereira, K., Boukabara, S., and Brown, P.: Atmospheric radiative transfer modeling: a summary of the AER codes, J. Quant. Spectrosc. Ra., 91, 233–244, 2005. 18430

Clough, S. A., Iacono, M. J., and Moncet, J.-L.: Line-by-line calculations of atmospheric fluxes and cooling rates: application to water vapor, J. Geophys. Res.-Atmos., 97, 15761–15785, 1992. 18430

Crevoisier, C., Clerbaux, C., Guidard, V., Phulpin, T., Armante, R., Barret, B., Camy-Peyret, C., Chaboureau, J.-P., Coheur, P.-F., Crépeau, L., Dufour, G., Labonnote, L., Lavanant, L., Hadji-Lazaro, J., Herbin, H., Jacquinet-Husson, N., Payan, S., Péquignot, E., Pierangelo, C., Sellitto, P., and Stubenrauch, C.: Towards IASI-New Generation (IASI-NG): impact of improved spectral resolution and radiometric noise on the retrieval of thermodynamic, chemistry and climate variables, Atmos. Meas. Tech. Discuss., 6, 11215–11277, doi:10.5194/amtd-6-11215-2013, 2013. 18440

Ellingson, R. G., Lee, H.-T., Yanuk, D. J., and Gruber, A.: A technique for estimating outgoing longwave radiation from HIRS radiance observations, J. Atmos. Ocean. Tech., 6, 706–711, 1989. 18426, 18430

Esposito, F., Grieco, G., Leone, L., Restieri, R., Serio, C., Bianchini, G., Palchetti, L., Pellegrini, M., Cuomo, V., Masiello, G., and Pavese, G.: REFIR/BB initial observations in the water vapour rotational band: results from a field campaign, J. Quant. Spectrosc. Ra., 103, 524–535, 2007. 18425

Goldberg, M., Ohring, G., Butler, J., Cao, C., Datla, R., Doelling, D., Gärtner, V., Hewison, T., Iacovazzi, B., Kim, D., Kurino, T., Lafeuille, J., Minnis, P., Renaut, D., Schmetz, J., Tobin, D., Wang, L., Weng, F., Wu, X., Yu, F., Zhang, P., and Zhu, T.: The Global Space-based Inter-Calibration System, B. Am. Meteorol. Soc., 92, 467–475, 2011. 18432

Goody, R., Anderson, J., and North, G.: Testing climate models: an approach, B. Am. Meteorol. Soc., 79, 2541–2549, 1998. 18422

ACPD
14, 18421–18459, 2014

Green, P. D., Newman, S. M., Beeby, R. J., Murray, J. E., Pickering, J. C., and Harries, J. E.: Recent advances in measurement of the water vapour continuum in the far-infrared spectral region, Philos. T. R. Soc. A, 370, 2637–2655, 2012. 18423, 18425

Gruber, A.: Determination of the Earth–atmosphere radiation budget from NOAA satellite data, Unknown, 1, NOAA Technical Report. NESS76, NOAA, U.S. Department of Commerce, Washington DC, 28 pp., 1977. 18426

Gruber, A. and Winston, J.: Earth–atmosphere radiative heating based on NOAA scanning radiometer measurements, B. Am. Meteorol. Soc., 59, 1570–1573, 1978. 18426

Hanel, R., Conrath, B., Kunde, V., Prabhakara, C., Revah, I., Salomonson, V., and Wolford, G.: The Nimbus 4 infrared spectroscopy experiment: 1. Calibrated thermal emission spectra, J. Geophys. Res., 77, 2629–2641, 1972. 18425

Hanel, R., Conrath, B., Jennings, D., and Samuelson, R.: Exploration of the Solar System by Infrared Remote Sensing, Cambridge Univ. Press, Cambridge, 2003. 18426

Harries, J., Brindley, H. E., Sagoo, P. J., and Bantges, R. J.: Increases in greenhouse forcing inferred from the outgoing longwave radiation spectra of the Earth in 1970 and 1997, Nature, 410, 355–357, 2001. 18422

Harries, J., Carli, B., Rizzi, R., Serio, C., Mlynczak, M., Palchetti, L., Maestri, T., Brindley, H., and Masiello, G.: The far-infrared earth, Rev. Geophys., 46, RG4004, doi:10.1029/2007RG000233, 2008. 18423, 18424, 18436, 18440

Huang, X., Ramaswamy, V., and Schwarzkopf, M. D.: Quantification of the source of errors in AM2 simulated tropical clear-sky outgoing longwave radiation, J. Geophys. Res.-Atmos., 111, D14107, doi:10.1029/2005JD006576, 2006. 18427

Huang, X., Yang, W., Loeb, N. G., and Ramaswamy, V.: Spectrally resolved fluxes derived from collocated AIRS and CERES measurements and their application in model evaluation: clear sky over the tropical oceans, J. Geophys. Res.-Atmos., 113, D09110, doi:10.1029/2007JD009219, 2008. 18427, 18440

Huang, X., Loeb, N., and Yang, W.: Spectrally resolved fluxes derived from collocated AIRS and CERES measurements and their application in model evaluation: 2. Cloudy sky and band-by-band cloud radiative forcing over the tropical oceans, J. Geophys. Res., 115, D21101, doi:10.1029/2010JD013932 2010. 18427

Huang, X., Cole, J. N., He, F., Potter, G. L., Oreopoulos, L., Lee, D., Suarez, M., and Loeb, N. G.: Longwave band-by-band cloud radiative effect and its application in GCM evaluation, J. Climate, 26, 450–467, 2013. 18427

ACPD
14, 18421–18459, 2014

Huang, Y., Ramaswamy, V., and Soden, B.: An investigation of the sensitivity of the clear-sky outgoing longwave radiation to atmospheric temperature and water vapor, J. Geophys. Res., 112, D05104, doi:10.1029/2005JD006906 2007. 18423
Lee, H., Gruber, A., Ellingson, R., and Laszlo, I.: Development of the HIRS outgoing longwave radiation climate dataset, J. Atmos. Ocean. Tech., 24, 2029–2047, 2007. 18426
Loeb, N., Priestley, K. J., Kratz, D. P., Geier, E. B., Green, R. N., Wielicki, B. A., Hinton, P. O., and Nolan, S. K.: Determination of unfiltered radiances from the Clouds and the Earth's Radiant Energy System instrument, J. Appl. Meteorol., 40, 822–835, 2001. 18431
Loeb, N., Manalo-Smith, N., Kato, S., Miller, W. F., Gupta, S. K., Minnis, P., and Wielicki, B. A.: Angular distribution models for top of atmosphere radiative flux estimation from the Clouds and the Earths Radiant Energy System Instrument on the Tropical Rainfall Measuring Mission satellite. Part I Methodology., J. Appl. Meteorol., 42, 240–265, 2003. 18428
Loeb, N., Wielicki, B., Doelling, D., Smith, G., Keyes, D., Kato, S., Manalo-Smith, N., and Wong, T.: Toward optimal closure of the Earth's top-of-atmosphere radiation budget, J. Climate, 22, 748–766, 2009. 18432
Maestri, T. and Rizzi, R.: A study of infrared diabatic forcing of ice clouds in the tropical atmosphere, J. Geophys. Res., 108, 4139, doi:10.1029/2002JD002146, 2003. 18424
Masiello, G., Serio, C., Esposito, F., and Palchetti, L.: Validation of line and continuum spectroscopic parameters with measurements of atmospheric emitted spectral radiance from far to mid infrared wave number range, J. Quant. Spectrosc. Ra., 113, 1286–1299, 2012. 18425
Minnis, P., Young, D. F., Sun-Mack, S., Heck, P. W., Doelling, D. R., and Trepte, Q. Z.: CERES cloud property retrievals from imagers on TRMM, Terra, and Aqua, in: Remote Sensing, International Society for Optics and Photonics, Barcelona, Spain, 37–48, 2004. 18431
Miskolczi, F. M. and Mlynczak, M. G.: The greenhouse effect and the spectral decomposition of the clear-sky terrestrial radiation, Quarterly Journal of the Hungarian Meteorological Service, 108, 209–251, 2004. 18424
Mlynczak, M., Johnson, D., Bingham, G., Jucks, K., Traub, W., Gordley, L., and Harries, J.: The far-infrared spectroscopy of the troposphere (FIRST) project, Proc. SPIE, 5659, 81–87, 2004. 18423, 18425
Mlynczak, M., Johnson, D., Latvakoski, H., Jucks, K., Watson, M., Kratz, D., Bingham, G., Traub, W., Wellard, S., Hyde, C. and Liu, X.: First light from the Far-Infrared Spectroscopy of the Troposphere (FIRST) instrument, Geophys. Res. Lett., 33, L07704, doi:10.1029/2005GL025114 2006. 18425

ACPD
14, 18421–18459, 2014

National Research Council: Earth Science and Applications from Space: National Imperatives for the Next Decade and Beyond, National Academies Press, Washington, DC, 2007. 18425
Ohring, G., Gruber, A., and Ellingson, R.: Satellite determinations of the relationship between total longwave radiation flux and infrared window radiance, J. Clim. Appl. Meteorol., 23, 416–425, 1984. 18426
Palchetti, L., Bianchini, G., Carli, B., Cortesi, U., and Del Bianco, S.: Measurement of the water vapour vertical profile and of the Earth's outgoing far infrared flux, Atmos. Chem. Phys., 8, 2885–2894, doi:10.5194/acp-8-2885-2008, 2008. 18425
Phillips, N., Susskind, J., and McMillin, L.: Results of a joint NOAA/NASA sounder simulation study, J. Atmos. Ocean. Tech., 5, 44–56, 1988. 18430
Priestley, K., Wielicki, B., Green, R., Haeffelin, M., Lee, R., and Loeb, N.: Early radiometric validation results of the CERES Flight Model 1 and 2 instruments onboard NASA'S Terra Spacecraft, Adv. Space Res., 30, 2371–2376, 2002. 18431
Rizzi, R. and Mannozzi, L.: Preliminary results on the planetary emission between 100 and 600 cm^{-1}, REFIR Radiation Explorer in the Far Infrared Final Rep ENV4 CT6, Eur. Comm., Brussels, 344, 77–88, 2000. 18424
Rizzi, R., Serio, C., and Amorati, R.: Sensitivity of broadband and spectral measurements of outgoing radiance to changes in water vapor content, in: International Symposium on Optical Science and Technology, International Society for Optics and Photonics, San Diego, CA, USA, 29 July 2001, 181–190, 2002. 18423
Shine, K. P., Ptashnik, I. V., and Rädel, G.: The water vapour continuum: brief history and recent developments, Surv. Geophys., 33, 535–555, 2012. 18423
Simeoni, D., Astruc, P., Miras, D., Alis, C., Andreis, O., Scheidel, D., Degrelle, C., Nicol, P., Bailly, B., Guiard, P., Clauss, A., Blumstein, D., Maciaszek, T., Chalon, G., Carlier, T., and Kayal, G.: Design and development of IASI instrument, Optical Science and Technology, the SPIE 49th Annual Meeting, International Society for Optics and Photonics, Denver, CO, 2 August, 208–219, 2004. 18429
Sinha, A. and Harries, J. E.: Water vapour and greenhouse trapping: the role of far infrared absorption, Geophys. Res. Lett., 22, 2147–2150, 1995. 18424
Soden, B. and Held, I.: An assessment of climate feedbacks in coupled ocean–atmosphere models, J. Climate, 19, 3354–3360, 2006. 18423

ACPD
14, 18421–18459, 2014

Sun, F., Goldberg, M. D., Liu, X., and Bates, J. J.: Estimation of outgoing longwave radiation from Atmospheric Infrared Sounder radiance measurements, J. Geophys. Res.-Atmos., 115, D09103, doi:10.1029/2009JD012799 2010. 18426

Thomas, S. and Priestley, K.: CERES FM1–FM6 Instrument Update, Spring 2014 CERES Science Team Meeting, Hampton, 22–24 April, VA, 2014. 18432

Turner, D. D., Tobin, D., Clough, S. A., Brown, P. D., Ellingson, R. G., Mlawer, E. J., Knuteson, R. O., Revercomb, H. E., Shippert, T. R., Smith, W. L., and Shephard, M. W.: The QME AERI LBLRTM: a closure experiment for downwelling high spectral resolution infrared radiance, J. Atmos. Sci., 61, 2657–2675, 2004. 18425

Wielicki, B., Barkstrom, B., Harrison, E., Lee III, R., Louis Smith, G., and Cooper, J.: Clouds and the Earth's Radiant Energy System (CERES): an earth observing system experiment, B. Am. Meteorol. Soc., 77, 853–868, 1996. 18431

ACPD
14, 18421–18459, 2014

Table 1. Instantaneous biases between CERES and IASI OLR at SNO events with standard errors. Units are $W\,m^{-2}\,sr^{-1}$. Figures in brackets are relative differences between the bias and the mean radiation measured by both CERES and IASI.

	All times	Day	Night
Both	0.33 ± 0.11 (0.50 %)	0.61 ± 0.17 (0.95 %)	−0.02 ± 0.14 (0.01 %)
Aqua	0.33 ± 0.14 (0.57 %)	0.48 ± 0.20 (0.78 %)	0.11 ± 0.19 (0.25 %)
Terra	0.32 ± 0.18 (0.50 %)	0.76 ± 0.28 (1.15 %)	−0.12 ± 0.2 (−0.17 %)

ACPD
14, 18421–18459, 2014

Table 2. Global mean biases between IASI OLR and CERES instruments for April 2012. Units are $W\,m^{-2}\,sr^{-1}$. Figures in brackets are relative differences between the bias and the mean radiation measured by both CERES and IASI. Italic figures in brackets are the biases split by land and ocean respectively.

	All times	Day	Night
Aqua CERES – IASI			
All-sky	0.79 (0.94 %)	1.44 (1.65 %)	0.16 (0.18 %)
Clear-sky	1.14 (1.03 %)	3.03 (3.00 %)	0.46 (0.22 %)
Terra CERES – IASI			
All-sky	1.04 (1.26 %)	1.40 (1.65 %)	0.70 (0.87 %)
Clear-sky	1.23 (1.23 %)	1.80 (1.81 %)	1.16 (1.15 %)
Terra – Aqua CERES			
All-sky	0.26 (0.32 %)	−0.04 (−0.01 %)	0.54 (0.69 %)
Clear-sky	0.08 (0.17 %)	1.28 (1.27 %)	0.72 (0.94 %)

ACPD
14, 18421–18459, 2014

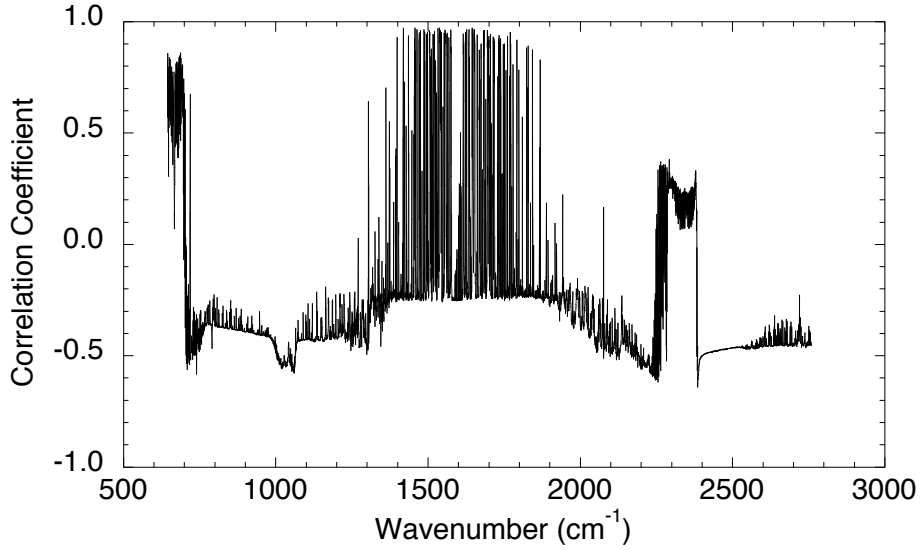

Figure 1. Linear correlation coefficients between the radiance at 25.25 cm^{-1} and the rest of the spectrum. Data is simulated by the LBLRTM from Phillips Soundings.

ACPD
14, 18421–18459, 2014

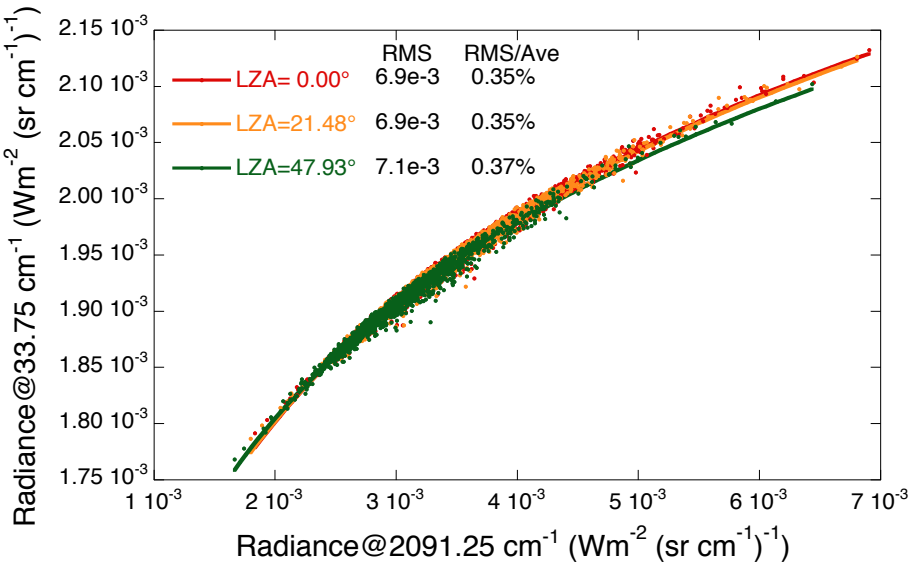

Figure 2. Relationship of radiances at 33.75 and 2091.25 cm^{-1} simulated by LBLRTM from Phillips Soundings, where the scatter points and fitting curve are based on data for local zenith angle 0° (red), 21.48° (orange), and 47.93° (green), respectively. Units are $W\,m^{-2}\,sr^{-1}\,(cm^{-1})^{-1}$.

ACPD
14, 18421–18459, 2014

Can IASI be used to simulate the total spectrum of outgoing longwave radiation?

E. C. Turner et al.

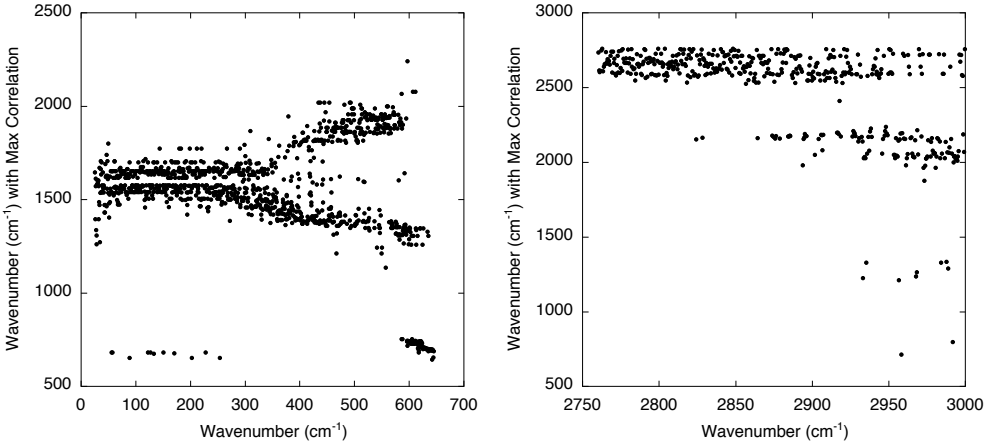

Figure 3. The wavenumbers of IASI observed radiance spectrum (*y* axis) that show empirically the maximum correlation coefficients for the FIR (left) and NIR (right) wavenumbers (*x* axis), based on a log–log transformation.

ACPD
14, 18421–18459, 2014

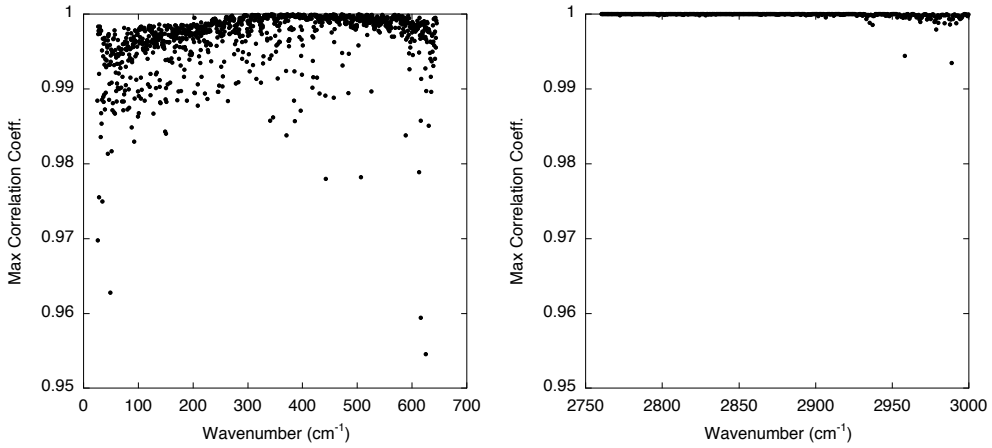

Figure 4. The maximum correlation coefficients between wavenumbers in the FIR (left) and NIR (right) and the corresponding predictor wavenumbers shown in Fig. 3.

ACPD
14, 18421–18459, 2014

Can IASI be used to simulate the total spectrum of outgoing longwave radiation?

E. C. Turner et al.

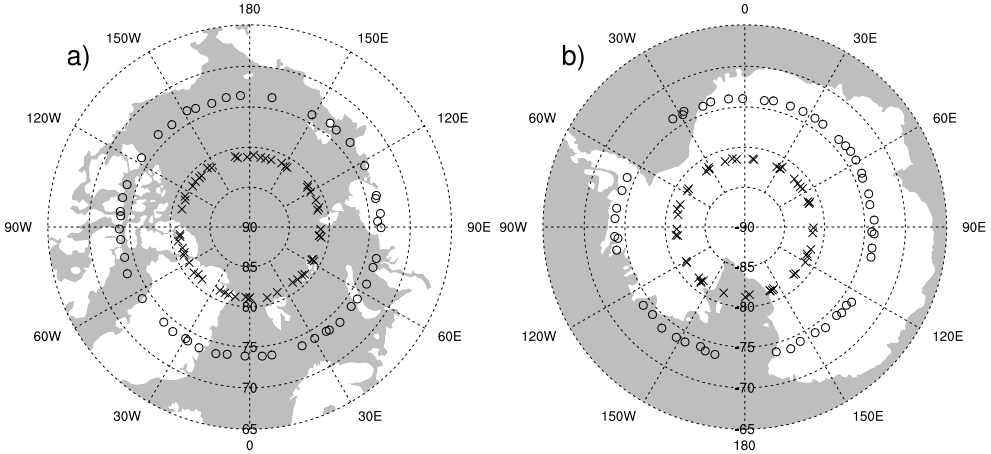

Figure 5. Locations of nearest nadir viewing SNOs, chosen as described in Sect. 2.4 between Metop-A and Terra (inner crosses) and Aqua (outer circles) for **(a)** the Arctic, and **(b)** Antarctic, for 2012.

ACPD
14, 18421–18459, 2014

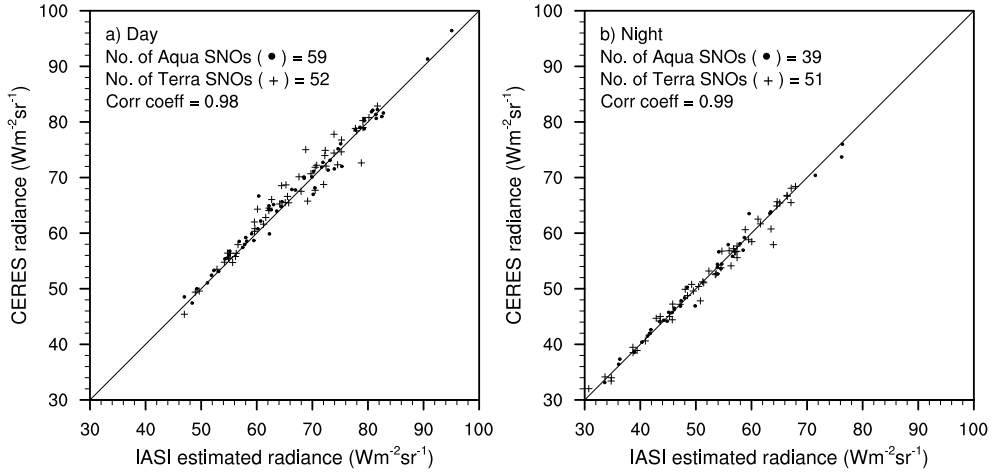

Figure 6. Absolute values of instantaneous LW radiances constructed from IASI on Metop-A against CERES measurements for both the Terra and Aqua satellites at closest SNO events for 2012 for **(a)** day, and **(b)** night.

ACPD
14, 18421–18459, 2014

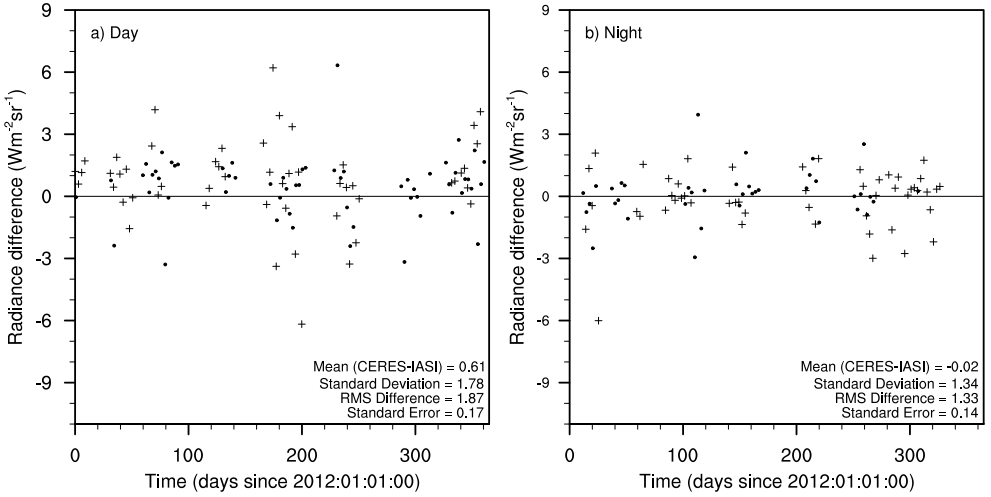

Figure 7. Time series of LW radiance bias at SNOs between CERES and IASI for 2012 for **(a)** day and **(b)** night. CERES measurements from Terra are marked with crosses and those from Aqua are shown as dots.

ACPD
14, 18421–18459, 2014

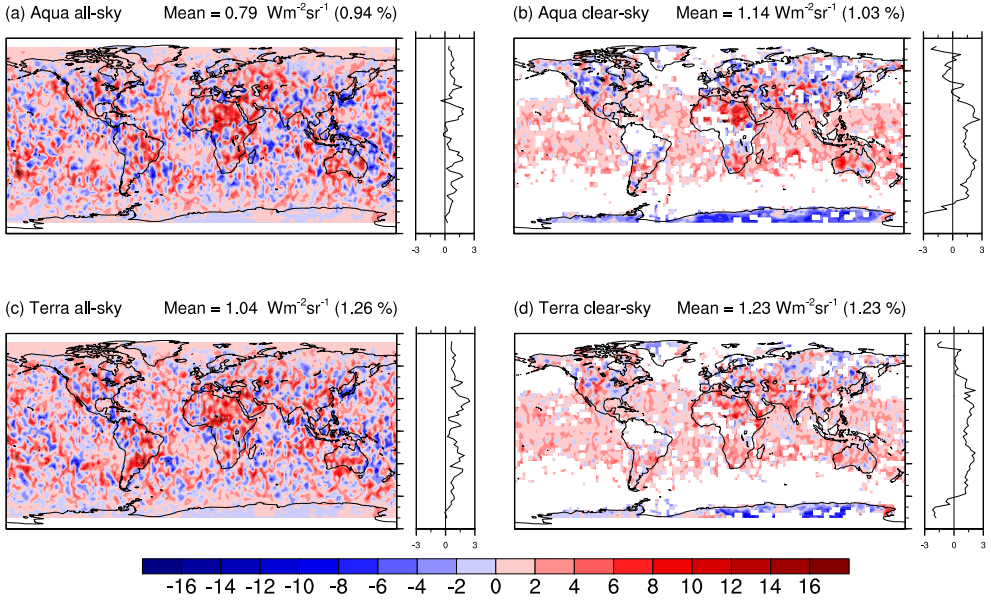

Figure 8. Differences between monthly gridded and averaged total LW radiances (CERES - IASI) at all available local times in April 2012 for: **(a)** Aqua all-sky, **(b)** Aqua clear-sky, **(c)** Terra all-sky, and **(d)** Terra clear-sky. Zonal means are shown to the right. Units are $\mathrm{W\,m^{-2}\,sr^{-1}}$. Figures in brackets are relative differences between the bias and the mean radiation measured by both CERES and IASI.

ACPD
14, 18421–18459, 2014

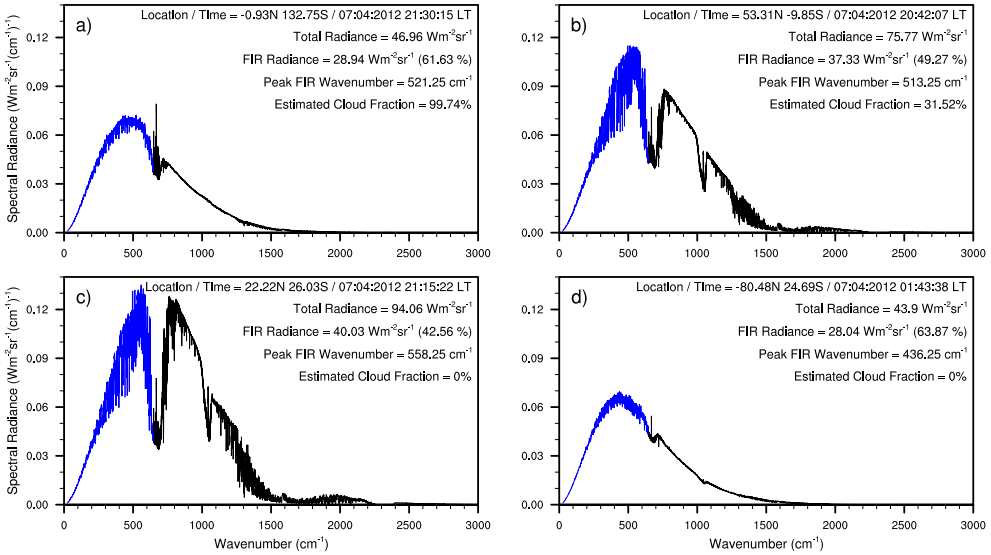

Figure 9. The total outgoing longwave spectral radiance (25.25–2999.75 cm^{-1}) constructed from IASI measurements (black) and estimated far infrared radiances (blue) for 4 instantaneous scenes over: **(a)** tropical rainforest, **(b)** midlatitude land, **(c)** Sahara desert, and **(d)** Antarctica. All are night-time scenes from the 7 April 2012.

ACPD
14, 18421–18459, 2014

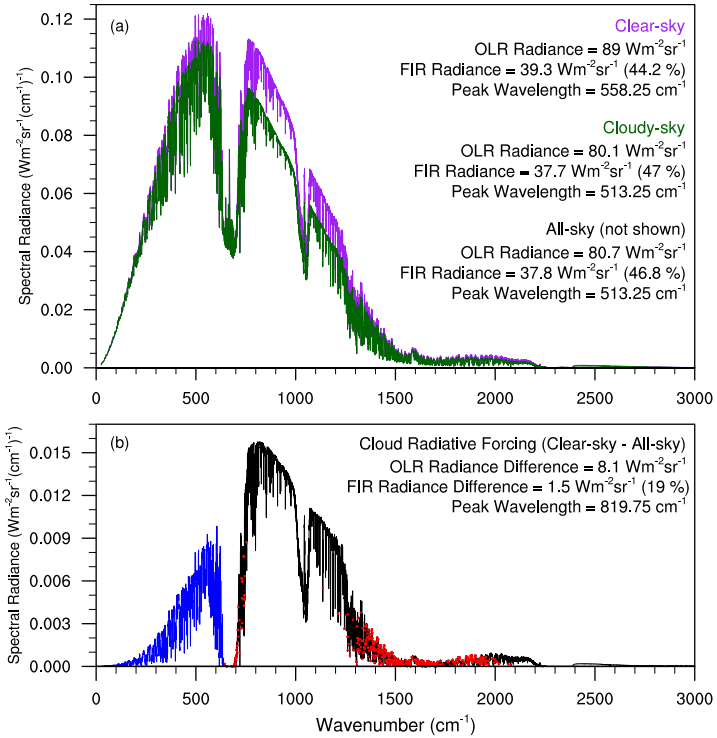

Figure 10. The outgoing longwave spectral radiance constructed from IASI data globally averaged for: **(a)** clear (purple) and cloudy (green) pixels. Numbers in parentheses are the fractional FIR contributions to the total LW broadband OLR. The all-sky curve would lie between the clear and cloudy curves but is not plotted for clarity. **(b)** The difference between clear-sky and all-sky (CRF) constructed from IASI measurements (black) and estimated far infrared radiances (blue) from predictor wavelengths in the mid infrared with the highest correlations (red dots). The number in parentheses is the fractional contribution of the FIR CRF to the total LW broadband CRF. Data is the area weighted monthly mean of April 2012.

ACPD
14, 18421–18459, 2014

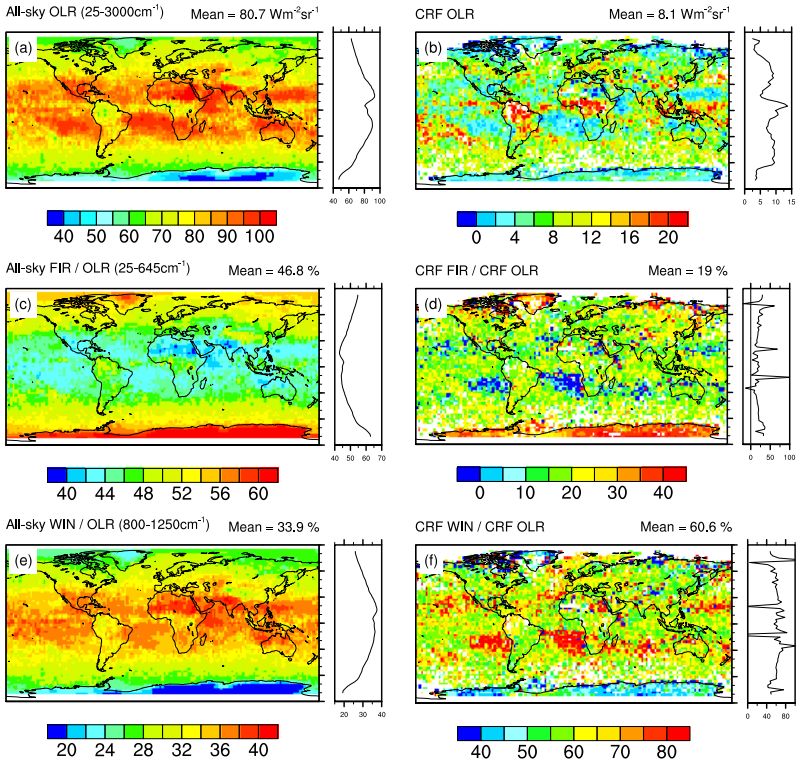

Figure 11. outgoing LW radiance maps created from all April 2012 pixels binned to a 2.5 by 2.5 grid and averaged. Zonal means are shown to the right of each map. On the left hand side we have all-sky: **(a)** total OLR, **(c)** FIR as a percentage of OLR, **(e)** window region as a percentage of OLR. On the right we have CRF (clear-sky – all-sky) for: **(b)** OLR, **(d)** the percentage of OLR that is FIR in the CRF, **(f)** the percentage of OLR that is in the window region in the CRF. Note that the colour scales are different for every panel. Missing data is shown in white.

ACPD
14, 18421–18459, 2014